

# Characterizing quasars in the mid-infrared: high signal-to-noise ratio spectral templates

Allison R. Hill,<sup>1</sup>★ S. C. Gallagher,<sup>1</sup> R. P. Deo,<sup>1</sup> E. Peeters<sup>1,2</sup>  
and Gordon T. Richards<sup>3,4</sup>

<sup>1</sup>The University of Western Ontario, 1151 Richmond Street, London, ON N6A3K7, Canada

<sup>2</sup>SETI Institute, 189 Bernardo Avenue, Suite 100, Mountain View, CA 94043, USA

<sup>3</sup>Department of Physics, 3141 Chestnut Street, Drexel University, Philadelphia, PA 19104, USA

<sup>4</sup>Max Planck Institut für Astronomie, Königstuhl 17, D-69117 Heidelberg, Germany

Accepted 2013 December 3. Received 2013 November 11; in original form 2013 July 19

## ABSTRACT

Mid-infrared (MIR) quasar spectra exhibit a suite of emission features including high ionization coronal lines from the narrow-line region illuminated by the ionizing continuum, broad dust bumps from silicates and graphites, and polycyclic aromatic hydrocarbon (PAH) features from star formation in the host galaxy. However, in *Spitzer* Infrared Spectrograph (IRS) data, few features are detected in most individual spectra because of typically low signal-to-noise ratios (S/N). By generating spectral composites from over 180 IRS observations of Sloan Digital Sky Survey broad-line quasars, we boost the S/N and reveal features in the complex spectra that are otherwise lost in the noise. In addition to an overall composite, we generate composites in three different luminosity bins that span the range of 5.6  $\mu\text{m}$  luminosities of  $10^{40}$ – $10^{46}$  ( $\text{erg s}^{-1}$ ). We detect the high-ionization, forbidden emission lines of [S IV], [O IV] and [Ne V]  $\lambda 14 \mu\text{m}$  in all templates and PAH features in all but the most luminous template. Ratios of lines with a range of ionization potentials show no evidence for a strong difference in the shape of the 41–97 eV ionizing continuum over this range of luminosities. The scaling of the emission-line luminosities as a function of continuum luminosity is consistent with what is expected, and shows no indication of a ‘disappearing narrow-line region’. The broad 10 and 18  $\mu\text{m}$  silicate features in emission increase in strength with increasing luminosity, and a broad 3–5  $\mu\text{m}$  blackbody consistent with graphite emission at 750 K is evident in the highest luminosity template. We find that the intrinsic quasar continua for all luminosity templates are consistent; apparent differences arise primarily from host galaxy contamination most evident at low luminosity.

**Key words:** accretion, accretion discs – quasars: emission lines – quasars: general – infrared: galaxies.

## 1 INTRODUCTION

Quasars – growing supermassive black holes in the centres of massive galaxies – are the subset of active galactic nuclei (AGNs) that constitute the most luminous objects in the Universe. They radiate substantial power across much of the electromagnetic spectrum, with the source of radiation in each frequency regime originating from a different location with respect to the supermassive black hole. The shape of a quasar’s spectral energy distribution (SED) can reveal much about the structure of the black hole–accretion disc system. Prior to the sensitivity of *Spitzer* in the mid-infrared (MIR), quasar SEDs covering this wavelength regime could only be constructed for small samples of the brightest objects. Elvis et al.

(1994) used multiwavelength photometry of 47 objects to generate a mean quasar SED which covered much of the electromagnetic spectrum (from radio to hard X-rays). The average SED showed some characteristic continuum features including the UV and MIR ‘bumps’. The source of the UV bump is best explained as optically thick continuum emission from the accretion disc itself (e.g. Malkan & Sargent 1982). The MIR bump is the thermal emission from dust grains heated by the accretion disc continuum. For dust to survive, the source of this emission must be at much greater distances ( $\geq 1$  pc) from the black hole than the accretion disc.

Quasars and AGN can be classified as Type 1 or Type 2 based on the absence (Type 2) or presence (Type 1) of broad emission lines in their optical spectra. The most persistent model to explain this difference in recent decades includes a dusty torus, that when viewed close to edge-on obscures the broad-line region close to the

★E-mail: [ahill49@gmail.com](mailto:ahill49@gmail.com)

central black hole (e.g. Antonucci 1993; Urry & Padovani 1995). This unified model implies no inherent difference between Type 1 and Type 2 objects; the effect is merely geometric. (The dynamical stability of the torus is an issue which is not addressed in the aforementioned unification picture.) An alternative view to simple unification is that the obscuring ‘torus’ is actually an outflow of dusty material from a disc wind (e.g. Konigl & Kartje 1994; Elitzur & Shlosman 2006; Keating et al. 2012). In this picture, the differences between Type 1 and Type 2 objects may not be purely geometric (e.g. if the dust distribution is patchy) and/or may have a dependence on evolution or accretion rate (or both). Dusty torus or not, there exists a distance from the black hole–accretion disc system where temperatures are low enough that dust can survive; this distance from the central engine is the dust sublimation radius ( $R_{\text{sub}}$ ). Beyond this point, the dust may be heated by and thus reprocess emission from the accretion disc, achieving peak temperatures of 100–1500 K (e.g. Antonucci 1993). At these temperatures, the peak of the emission will be in the MIR, thus accounting for the continuum emission of the MIR bump present in quasar SEDs (e.g. Elvis et al. 1994).

The depth and sky coverage of *Spitzer* photometry enabled the construction of multiwavelength quasar SEDs from larger and more complete samples. From 259 objects, Richards et al. (2006a) created average SEDs, binning the data to search for trends with parameters such as luminosity, radio-loudness and optical colour. They found the SEDs to be very similar with the exception of a near-infrared excess at  $\sim 4 \mu\text{m}$  in the most luminous quasars [a difference also noted by Hatziminaoglou et al. (2005) in a smaller sample of 35 objects]. This excess flux detected in the near-IR spectra of some AGN has been noted in the literature for decades (Edelson & Malkan 1986). More recently, Gallagher et al. (2007) observed the same bump in a sample of 234 quasars as a steepening of the spectral index in the 1–8  $\mu\text{m}$  range, explained as a thermal blackbody of hot graphite dust. Graphites have a higher dust sublimation temperature ( $\sim 1500 \text{ K}$ ) than the silicates which are the source of the 10 and 18  $\mu\text{m}$  features, and therefore have a smaller  $R_{\text{sub}}$  and are located closer to the central engine than silicates. While trying to model individual luminous quasar IRS spectra, Deo et al. (2011) found the fits often required a blackbody in the 2–8  $\mu\text{m}$  range with a temperature of  $\sim 1200 \text{ K}$ , further supporting the idea of a hot dust component.

Cooler dust emits thermal continuum at longer wavelengths overlaid with broad features roughly centred at 10 and 18  $\mu\text{m}$  from vibrational modes of silicate grains. Using *Spitzer* observations, Hao et al. (2005) detected both the 10 and 18  $\mu\text{m}$  features in emission in a sample of Type 1 PG quasars. This result seemed to support the picture proposed by Antonucci (1993) with the silicates in emission caused by a viewing angle of the ‘torus’ which is face-on in Type 1 objects, where the inner wall of the torus is illuminated (as opposed to an edge-on view where the column density is much higher and the silicates are seen in absorption).

In addition to the thermal continuum emission in the MIR, high-ionization emission lines from the forbidden transitions of ions such as [S IV], [O IV] and [Ne V] were expected (Spinoglio & Malkan 1992) from the ionization and excitation of the low-density host galaxy ISM by the UV through soft X-ray continuum of the accretion disc that is not blocked by the ‘torus’. Many of the high ionization lines predicted by Spinoglio & Malkan (1992) were observed in *ISO* studies (Genzel et al. 1998), and early spectra of MIR bright quasars from *Spitzer* (e.g. Weedman et al. 2005). While there have been many studies of emission line properties from the narrow lines in nearby AGNs (e.g. Keremdjiev, Hao & Charmandaris

2009; Pereira-Santaella et al. 2010; Dasyra et al. 2011), the studies of archetypal luminous quasars at  $z \sim 1\text{--}2$  have largely been limited to continuum studies; as an example, Deo et al. (2011) detected no forbidden lines in their 25 IRS spectra due to the relatively low signal-to-noise ratio (S/N) from these fainter objects.

It was not until recently that enough data have been gathered to perform a MIR spectroscopic statistical study. Because of the poor S/N in many spectra, it became almost a necessity to study features in quasars through spectral composites, as one of the only ways to reveal faint, ubiquitous features that would otherwise be lost in the noise. Hao et al. (2007) took a sample of 196 AGNs and ultra-luminous infrared galaxies (ULIRGs) from the *Spitzer* archive; of that subset, 24 were quasars, while the rest of the sample contained Seyferts (1 and 2) and ULIRGs. Average spectra were generated for each category of object, exhibiting the 10 and 18  $\mu\text{m}$  features in emission, along with weak detections of several MIR forbidden lines and PAH features. Compared to Seyferts and ULIRGs, the detected lines in the average luminous quasar spectrum (forbidden and PAH features alike) had smaller equivalent widths (EW).<sup>1</sup> The quasar continuum also increases to longer wavelengths more slowly (in units of  $L_{\nu}$  versus  $\lambda$ ) than the lower luminosity classes of objects – i.e. quasar spectra are ‘flatter’ (i.e. bluer) than Seyferts or ULIRGs. This is confirmed by Sargsyan et al. (2011), who compared the IR spectra of dusty starbursts and AGN and found ‘emission AGN’ (in reference to the 10  $\mu\text{m}$  feature) have flatter spectra than ‘absorption AGN’.

Quasars have been studied extensively in the optical/UV, as unobscured quasars are readily studied from the ground in this regime. Only space-based facilities such as *Spitzer* have the low background that allow them the sensitivity to detect similar objects in the MIR. As a result, the optical has the advantage of much larger sample sizes provided by the Sloan Digital Sky Survey (SDSS) quasar catalogue (Schneider et al. 2010), which contains over a hundred thousand quasars. Vanden Berk et al. (2001) used a sample of over 4000 Type 1 objects to generate spectral composites covering the rest-frame optical through UV. Their work determined canonical values for optical and UV line EWs and spectral indices. We extend this effort into the MIR for Type 1 quasars with a sample size of 184 objects – thus far unprecedented in the literature for this wavelength regime.

For this study, the assumed cosmology is  $H_0 = 70 \text{ km s}^{-1} \text{ Mpc}^{-1}$ ,  $\Omega_M = 0.3$  and  $\Omega_\Lambda = 0.7$ .

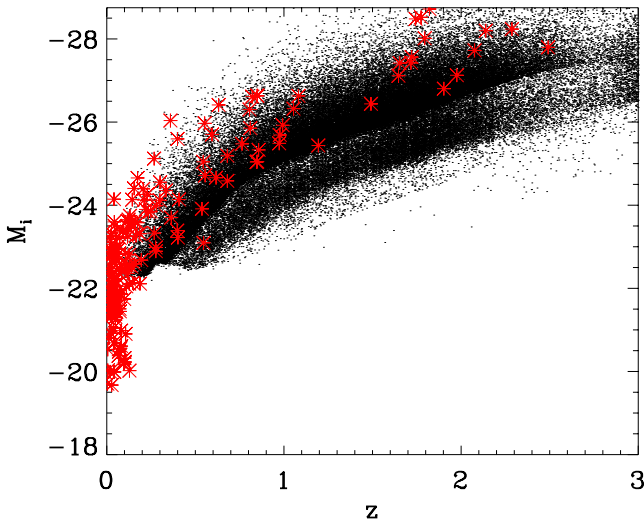
## 2 SAMPLE SELECTION

We coordinate cross matched the SDSS quasar catalogue (Schneider et al. 2010) with the *Spitzer* (Werner et al. 2004) Infrared Spectrograph (IRS; Houck et al. 2004) archive, using a match radius of 2 arcsec, yielding 184 low-resolution ( $R \sim 60\text{--}130$ ) MIR spectra (see Table 1). We selected all data which had short-low (SL; 5.1–14.3  $\mu\text{m}$ ) and/or long-low (LL; 13.9–39.9  $\mu\text{m}$ ) modules (although not all objects necessarily had both modules), opting to keep only the low-resolution data. Although our data span a wide range of luminosities ( $\log(L_{5.6 \mu\text{m}}) = 41.1\text{--}46.1 [\text{erg s}^{-1}]$ ) and redshifts ( $z = 0.001\text{--}2.49$ ), most of our objects occupy the low-luminosity (median of 43.9  $[\text{erg s}^{-1}]$  in log units), low-redshift (median of 0.081) regime of the parameter space (Fig. 1). The low-luminosity nature of our objects limits access to various parameters (e.g. virial

<sup>1</sup> This is reminiscent of the Baldwin Effect (Baldwin 1977) where the EW of the optical broad line C IV was shown to be anti-correlated with the optical continuum luminosity.

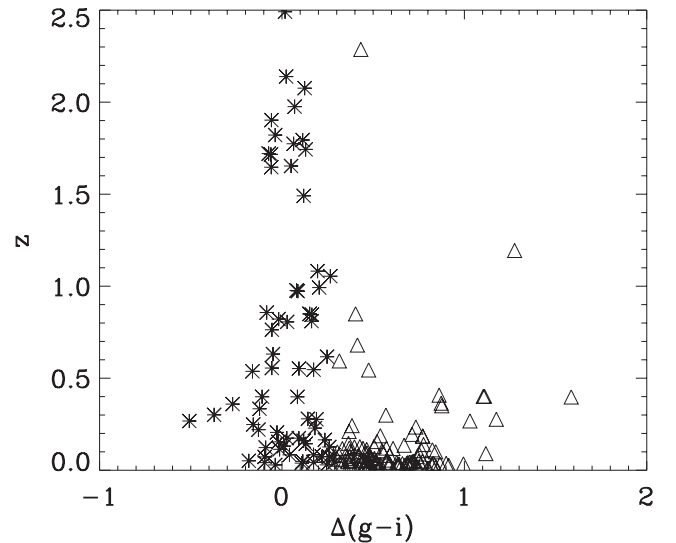
**Table 1.** *Spitzer* object summary (full table available in electronic format).

Object name <sup>a</sup>	SDSS identifiers			<i>Spitzer</i> identifiers		$z^b$	$\log(L_{5.6\ \mu\text{m}})$ [erg s <sup>-1</sup> ]	$M_i^c$	Template <sup>d</sup>
	plate	fid	mjd	aorkey	program ID				
FTM1113+1244	1604	566	53078	22391040	30119	0.680	46.095	-24.6	1
SDSSJ151307.75+605956.9	351	231	51695	14757376	50588	2.287	46.052	-28.2	1
SDSSJ170102.18+612301.0	613	365	52345	25977088	40936	1.821	46.013	-28.7	1
SDSSJ132120.48+574259.4	760	287	52264	18027776	40936	1.794	45.902	-28.0	1
SDSSJ024933.42-083454.4	1320	376	52759	25977344	3237	1.774	45.890	-28.5	1

<sup>a</sup>Objects are sorted in descending order of  $\log(L_{5.6\ \mu\text{m}})$ .<sup>b</sup>Redshifts taken from Hewett & Wild (2010).<sup>c</sup>Absolute  $i$ -band magnitude.<sup>d</sup>Number denotes which luminosity bin object resides in (where 1 is the most luminous group, 2 is the intermediate group and 3 is the least luminous group).**Figure 1.** Absolute,  $K$ -corrected (table 4; Richards et al. 2006b)  $i$ -band magnitudes from Shen et al. (2011) versus redshift. The black points correspond to the SDSS quasar catalogue (Shen et al. 2011;  $M_i < 22$ ). The red asterisks indicate the 184 objects of our sample, with the  $M_i$  values taken from the SDSS DR7 photometric catalogue (Abazajian et al. 2009).

black hole masses, and UV line luminosities) tabulated in quasar catalogues such as Hewett & Wild (2010) and Shen et al. (2011). For example, only 70 of our objects are in the Shen et al. (2011) catalogue.

A further possible bias in our sample is that 116 quasars have redder UV/optical colours compared to the sample of Richards et al. (2003), i.e. they are characterized by a more negative spectral index  $\alpha$  in  $f(\nu) \propto \nu^\alpha$ . Following the example of Richards et al. (2003), we calculated the relative  $g-i$  colours,  $\Delta(g-i)$  (Richards et al. 2001), of the quasars in our sample, and plotted them against their redshifts (Fig. 2). The relative colour accounts for the effects of redshift as prominent emission lines shift in and out of the SDSS bands, by determining the underlying continuum colour. The median colours of quasars at the redshift of each quasar are subtracted from the measured colour of each object. Adopting the same cut-off as Richards et al. (2003) we define ‘red’ quasars as those with  $\Delta(g-i) > 0.3$ . Using this definition, we find that the majority of our objects are classified as ‘red’ (Fig. 2). It is not clear if this ‘reddening’ is intrinsic to the quasar, or is a result of contamination from the host galaxy in our low-redshift sources. Spectral decomposition would be required to comment further on the nature of the dust

**Figure 2.** Redshift versus the relative  $g-i$  colour of the objects in our sample. Open triangles indicate quasars which are defined as ‘red’, in that  $\Delta(g-i) > 0.3$ . The objects with  $\Delta(g-i) < 0.3$  are defined as ‘normal’ (following the convention of Richards et al. 2003) and are represented as asterisks. The total number of objects classified as ‘red’ is 116.

reddening and/or host galaxy contamination in our low-luminosity, low-redshift objects.

### 3 DATA REDUCTION AND ANALYSIS

#### 3.1 *Spitzer* spectra

We obtained the basic calibrated data (BCD) products processed with the standard *Spitzer* IRS pipeline (version S18.7.0) from the *Spitzer* Science Center (SSC) archive. We cleaned the BCD images using the *IRSCLEAN* software package (part of the *SMART* Higdon et al. 2004; Lebouteiller et al. 2010 package) to fix rogue pixels using SSC supplied masks, and a weak thresholding of the pixel histogram to remove highly discrepant rogue pixels. We co-added the multiple data collection event (DCE) image files into one image for each module, spectral order and nod position (e.g. SL, first order, first nod position) using the ‘fair co-add’ option in *SMART* (Higdon et al. 2004; Lebouteiller et al. 2010). The co-added images from the opposite order/nod positions (as per setup of observation) were subtracted from each-other to remove the sky background in each.

The spectra were extracted using the ‘optimal extraction option’ within the *SMART* package. All the image combining and spectrum extraction operations were carried out using *SMART*. We checked our extractions using automated extractions with the *Spitzer* IRS Custom Extractor (*SPICE*) program also, and found good matches between extracted spectra. In the cases where the SL and LL spectra of the same object did not have the same average flux values where they overlapped in wavelength, we scaled the SL module spectra to the LL module spectra as the LL slit widths are larger than the SL slit widths (cf. Brandl et al. 2006).

### 3.2 Template construction

To prepare the spectra for averaging, the data need to be shifted to the rest frame and interpolated to a common wavelength scale. We use a bin size of 0.05  $\mu\text{m}$ . Next, an appropriate continuum point for normalization was selected to minimize overlap with significant features such as PAH emission, forbidden lines and broad silicate features. Spoon et al. (2007) devised methods to measure the flux densities of a wide variety of galaxies using the 5.6, 14 and 26  $\mu\text{m}$  locations as continuum points (chosen because they are relatively featureless regions of the spectrum). To highlight the differences in continuum in the red and blue end of the MIR, we chose 14  $\mu\text{m}$  as the normalization point as it effectively bisects the wavelength range considered. Not all of the objects contained flux information at 14  $\mu\text{m}$ , due to either redshift effects, or the absence of coverage of one or more of the *Spitzer* modules. To account for this, we took advantage of the fact that quasars have similarly shaped SEDs (Richards et al. 2006a). We utilized the multi-wavelength SED composite from Richards et al. (2006a), and normalized the data to the 5.6  $\mu\text{m}$  continuum point and extrapolated along the SED to calculate flux information at 14  $\mu\text{m}$ . Once shifted and normalized, the average template spectrum was calculated, with a  $3\sigma$ -clipped mean returned for each wavelength bin. The template constructed from all 186 objects can be found in Fig. 3.

To study the effects of luminosity on global trends, the luminosity at 5.6  $\mu\text{m}$  was calculated for each object. This continuum point was

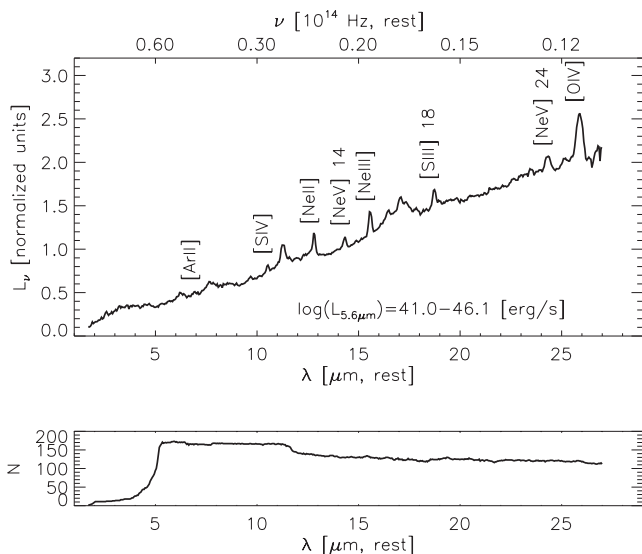


**Figure 3.** Top panel: rest-frame quasar template composed of all objects in the sample. Prominent narrow-line emission features are labelled. The 5.6  $\mu\text{m}$  luminosity range is indicated in the lower right. Bottom panel: number of objects contributing to the template in each wavelength bin.

chosen because it has the most overlap of the rest frame spectra, and is a better indicator of the quasar luminosity, as contamination from the host galaxy typically occurs at longer wavelengths in the MIR (Schweitzer et al. 2006). We opted for a MIR continuum point over an optical continuum point because of the large proportion of our objects which may suffer from host galaxy contamination and/or optical continuum reddening (Fig. 2). We suspect contamination from the host to be more noticeable in the optical over the 5.6  $\mu\text{m}$  continuum point, as can be seen in Fig. 4.

At the low-luminosity ( $L_{5.6\mu\text{m}} < 10^{43}$  erg s $^{-1}$ ) end of the distribution in Fig. 4, a large fraction of AGNs show an excess of  $M_i$  emission. This is likely a result of the significant contribution of host galaxy emission in the rest-frame  $i$  band. However, the 5.6  $\mu\text{m}$  continuum comes from hot (a few hundred to a thousand K) dust in the immediate vicinity of the quasar; these high temperatures are not typical of dust heated by star formation, and thus the host galaxy contribution is expected to be negligible. Therefore,  $\log(L_{5.6\mu\text{m}})$  is a better tracer of the intrinsic luminosity of the quasar. It is less clear what causes an excess of  $M_i$  compared to  $\log(L_{5.6\mu\text{m}})$  at the high-luminosity end in Fig. 4. However,  $M_i$  is an imperfect measure of optical luminosity, as it is calculated by assuming a typical  $K$ -correction from the observed optical photometry. The extrapolation from the observed photometry to  $M_i$  is larger at higher redshift, and the most luminous objects in our sample have (on average) significantly higher redshifts than the less luminous AGNs (see Fig. 1). Using the integrated optical and IR photometry of a sample of 234 SDSS quasars to determine  $L_{\text{opt}}$  and  $L_{\text{IR}}$  from Richards et al. (2006a), Gallagher et al. (2007) found that the ratio of the two was consistent with being constant as a function of luminosity once dust-reddening (which preferentially reduces the optical luminosity) was taken into account (see their fig. 2). Therefore, we do not consider the apparent ‘excess’ of optical luminosity as measured by  $M_i$  to indicate a true effect.

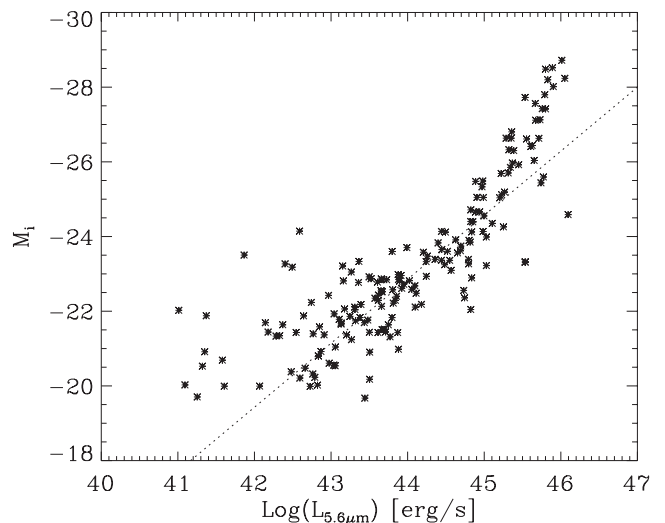


**Figure 4.** The absolute  $i$ -band magnitude,  $M_i$ , versus the  $L_{5.6\mu\text{m}}$  continuum luminosity, of each quasar. A line of slope 1 is overplotted (dashed line). At low luminosities there is greater scatter, with the values of  $M_i$  greater than would be expected with a 1:1 relation (assuming both continuum points trace the bolometric luminosity of the quasar). This likely results from the greater sensitivity of  $M_i$  to host galaxy contamination compared to  $L_{5.6\mu\text{m}}$ . At the high luminosity end, objects typically have high redshifts, and  $M_i$  is calculated from the observed-frame optical photometry with a typical  $K$ -correction, and therefore may not be an accurate tracer of the optical continuum luminosity.



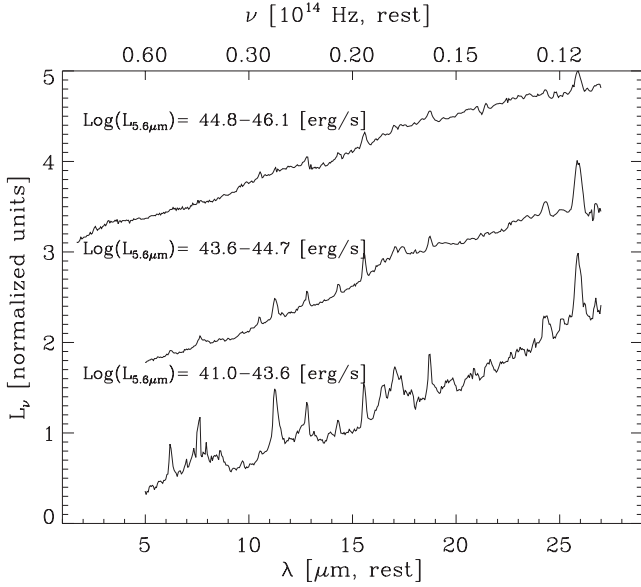


**Figure 5.** Rest-frame quasar composites of all three luminosity bins. Each template has been shifted in the ordinate for clarity, and the vertical location does not represent its true difference in  $L_v$ . The  $\log(L_{5.6\mu\text{m}})$  ranges of the objects that contributed to each bin are indicated above each template.

The objects were ordered according to  $\log(L_{5.6\mu\text{m}})$ , and equally divided into three bins (with each bin containing 61 objects) with the  $\log(L_{5.6\mu\text{m}})$  ranges for each tertile of 41.0–43.6, 43.6–44.7 and 44.8–46.1 [ $\text{erg s}^{-1}$ ], respectively. For each bin, a template spectrum was generated, as shown in Fig. 5 (all template spectra can be found in Table 2). Template spectra were also constructed for ‘reddened’ and ‘normal’ quasars according to their relative colour,  $\Delta(g - i)$ , (see Section 2) with no significant difference between them. We therefore conclude that the relative  $g - i$  colour does not notably affect the MIR spectra.

As previously mentioned, each of our objects with IRS spectra also has a counterpart in the SDSS quasar catalogue. We provide SDSS template spectra (Fig. 6), which were generated in the same manner as the IRS templates (i.e. using  $\sigma$  clipping), and binned according to their 5.6  $\mu\text{m}$  luminosity. For the SDSS templates, we use a bin size of 2  $\text{\AA}$ . Corresponding luminosity-binned template spectra are also provided (Fig. 7). The SDSS spectra cleaned of OH sky lines were taken from the Hewett & Wild (2010) quasar catalogue.

**Table 2.** Template spectra for all objects, and luminosity binned objects (full table available in electronic format).

$\lambda [\mu\text{m}]$	$L_v [\text{erg s}^{-1} \text{Hz}^{-1}, \text{normalized units}]$			
	$L_{v\text{tot}}$	$L_{v1}$	$L_{v2}$	$L_{v3}$
1.6909	0.1088	0.1088		
1.7409	0.1040	0.1040		
1.7909	0.1115	0.1115		
1.8409	0.1299	0.1299		

*Note.*  $L_{v\text{tot}}$  is the template for all objects.  $L_{v1}$ ,  $L_{v2}$ ,  $L_{v3}$  are the template spectra for the most luminous objects, the intermediate-luminosity objects and the least luminous objects, respectively. Blank values are due to a lack of wavelength coverage because of the dependence of the luminosity on redshift (coverage for other templates begins between 3 and 5  $\mu\text{m}$ ).

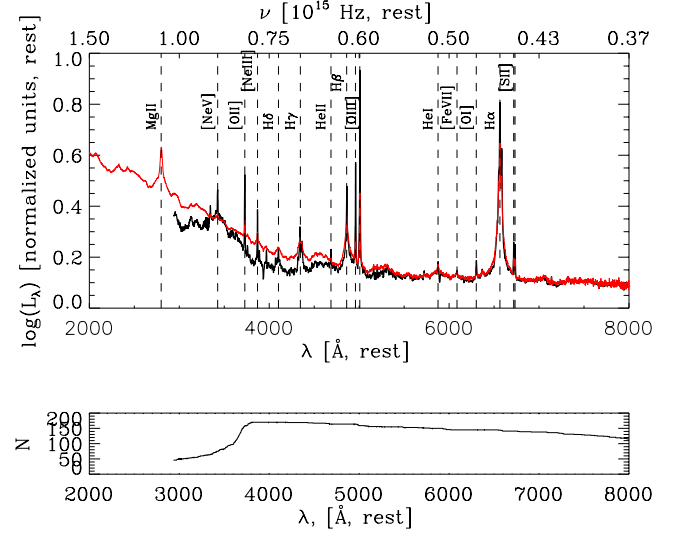


**Figure 6.** Top panel: rest-frame UV-optical quasar template of all objects in the sample (solid black line). Overplotted is the Vanden Berk et al. (2001) composite (solid red line), normalized to the flux at 7481  $\text{\AA}$ . Prominent emission lines are labelled. Bottom panel: number of objects contributing to the template in each wavelength bin. Our template is consistent with the Vanden Berk et al. (2001) composite at long wavelengths, but deviates at shorter wavelengths. The Vanden Berk et al. (2001) composite has a larger contribution from many higher redshift (and consequently higher luminosity) objects, particularly at short wavelengths. As more luminous quasars typically have bluer continua (e.g. Richards et al. 2002), the discrepancy between our composites shortwards of  $\sim 4600 \text{\AA}$  is not unexpected.

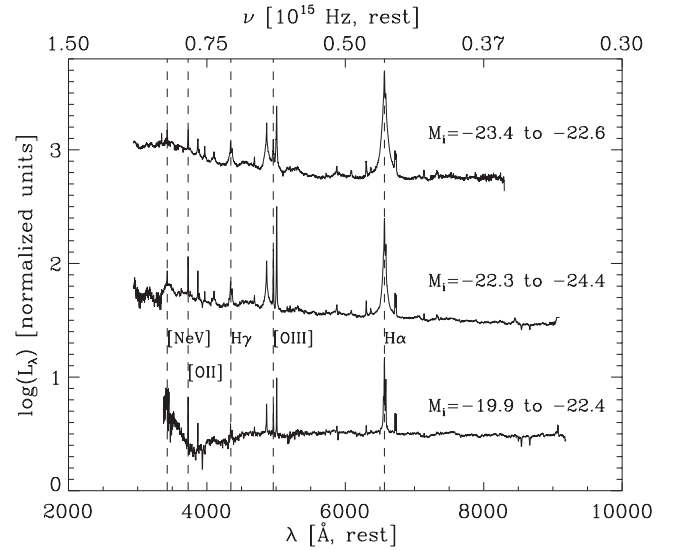


**Figure 7.** Rest-frame optical quasar templates. Each template has been shifted in the ordinate for clarity, and the vertical location does not reflect the true difference in  $L_v$ . The uppermost template contains the same objects as the uppermost template of Fig. 5. The range in  $M_i$  of the objects contributing to the template is labelled above each template.

### 3.3 MIR spectral fitting

For each MIR template, we calculated line luminosities, central wavelengths and EWs for the detected features which include narrow emission lines and PAHs. Because of the blending of PAH and narrow-line features in the composite, especially at shorter wavelengths, we utilized the spectral decomposition code PAHFIT

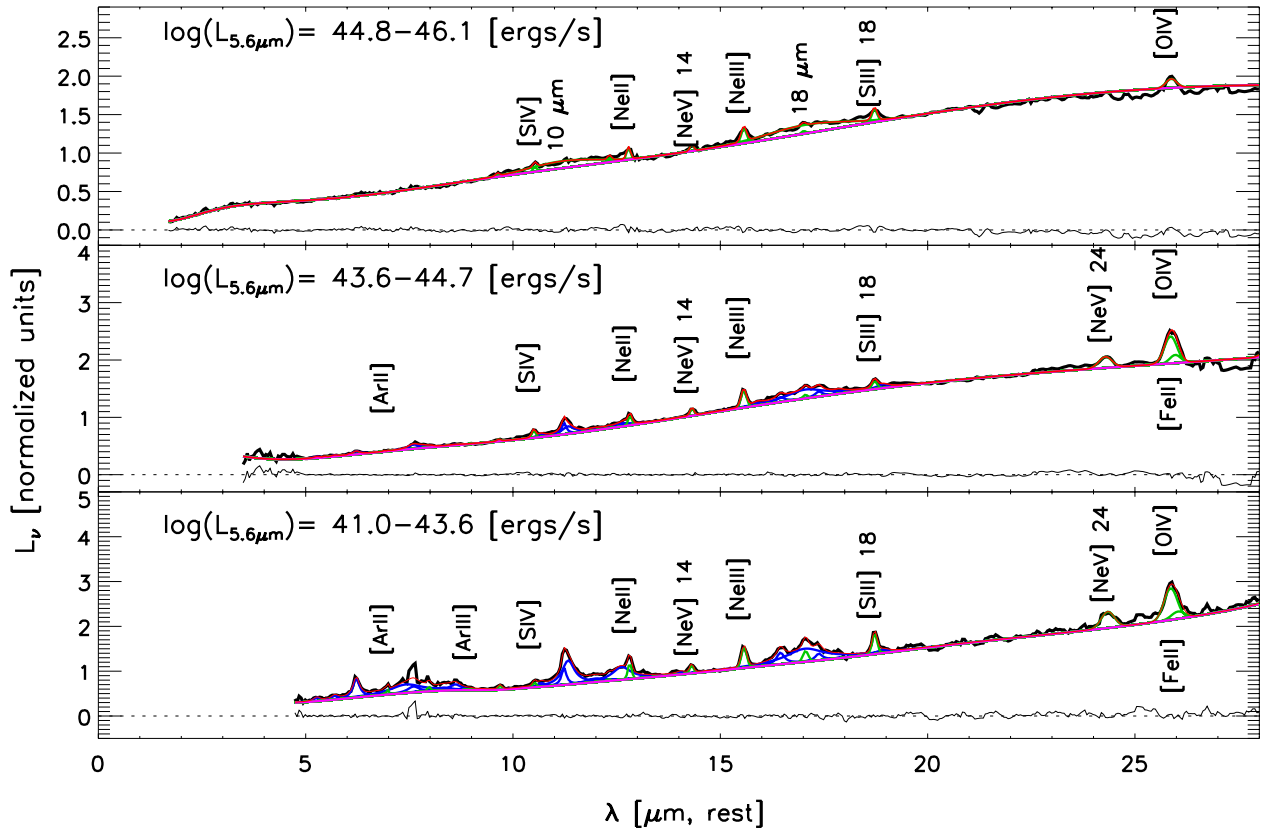


**Figure 8.** PAHFIT models of rest-frame templates, with residuals plotted (straddling the dotted black line at  $L_v = 0$ ). The top panel corresponds to the most luminous template, and the luminosity decreases towards the bottom panel. Green and blue curves show the narrow-line and PAH features, respectively. Magenta is the continuum fit, and red is the total model. Note the absence of PAH features in the top panel, and that the 10 and 18  $\mu\text{m}$  features only become visible in the top panel.

developed by Smith et al. (2007) to calculate the EWs, central wavelengths and relative intensities for MIR features. PAHFIT is an IDL script which uses least-squares minimization to de-convolve spectra into their continuum, dust and narrow-line components (see Smith et al. 2007 for details). Because PAHFIT was not designed with quasars and AGN in mind, it does not naturally fit warmer dust components such as silicates in emission. To compensate for this, two broad, Gaussian functions were added to fit the 10 and 18  $\mu\text{m}$  silicate features. The resulting fits for each composite appear in Fig. 8.

Using the PAHFIT-generated errors on the central intensity of each, we estimated the error of the narrow-line EWs by generating two Gaussians (as the narrow-line features are fit using Gaussians) with central peak intensities corresponding to the central intensity  $\pm$  the errors, and calculated the EWs of those Gaussians. These two values are the estimated upper and lower bounds for the PAHFIT-generated EWs.

## 4 RESULTS

### 4.1 Continuum trends

A comparison of the luminosity-binned templates of Figs 5 and 8 shows apparent trends with increasing luminosity. The continuum becomes flatter redwards of 20  $\mu\text{m}$  (i.e. the higher luminosity templates are MIR-bluer than the lower luminosity templates), which can be seen in Fig. 9. The flattening of the continuum with luminosity is gradual – the most luminous template is MIR-bluer than the

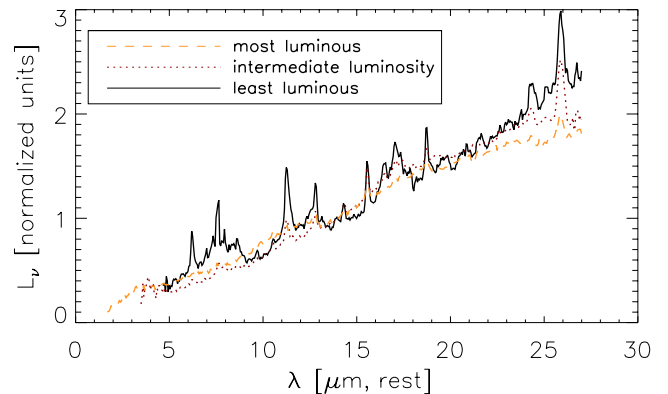


**Figure 9.** All luminosity binned templates plotted with no offsets (normalized to the template values at 14  $\mu\text{m}$ ). At longer wavelengths, the least luminous template (solid black line) rises to higher values than the intermediate-luminosity template (dotted red line) and the most luminous template (dashed orange line).

second most luminous template, and the least luminous template is MIR-redder than the second most luminous template. This continuum trend with increasing luminosity is consistent with the findings of Hao et al. (2007) who observed that the continua of quasars were flatter than the Seyferts in their sample.

The most luminous template was the only template to require the inclusion of silicates in emission at both 10 and 18  $\mu\text{m}$ . Also visible in the highest luminosity template is the 3  $\mu\text{m}$  (or NIR)

bump, which is likely caused by graphites located closer to the central engine, as graphites have a higher sublimation temperature ( $T_{\text{sub}} \sim 1500$  K) than silicates (Barvainis 1987). The presence of the  $3\text{ }\mu\text{m}$  bump in higher luminosity quasars is consistent with the anti-correlation between IR luminosity and the  $1\text{--}8\text{ }\mu\text{m}$  spectral index noted by Richards et al. (2006a) and Gallagher et al. (2007), and the requirement of a hot dust component in the SED fitting of Deo et al. (2011) and Mor & Netzer (2012). However, we are able to detect the NIR  $3\text{ }\mu\text{m}$  bump in the most luminous MIR template because our most luminous sources tend to have higher redshifts (Fig. 1); a fraction of the rest-frame spectra have the advantage of covering this range. Thus we cannot say for certain that this hot thermal dust emission is absent in the lower-luminosity sources.

#### 4.2 PAH features

PAH features were detected in all but the most luminous template (Fig. 8). If the most luminous template is supplied to PAHFIT with no constraints on the PAH features, there will be some PAH emission modelled in the  $5\text{--}15\text{ }\mu\text{m}$  region but almost no PAH emission in the  $15\text{--}20\text{ }\mu\text{m}$  range. Since very few sources exhibit this behaviour (Smith et al. 2007), we interpret this as an artefact of the software fitting the noise in the spectrum. We therefore constrain the parameters of PAHFIT to not include PAH features in the most luminous case, which is consistent with what is seen in the spectral composite.

For the templates which do show prominent PAH emission features, the combined EW of these features decreases with increasing  $5.6\text{ }\mu\text{m}$  luminosity, until they either are overwhelmed by the continuum emission, or are not present in the most luminous template. To determine how luminous the PAH emission would need to be in order to be seen above the noise we took the best-fitting PAH model shown in the bottom panel of Fig. 8 and added Gaussian noise ( $S/N = 14.5$ , chosen from the  $S/N$  at  $6.2\text{ }\mu\text{m}$ ). To check the most optimistic case, the PAH model was assumed to come from the highest luminosity object in the lowest luminosity bin ( $\log(L_{5.6\text{ }\mu\text{m}}) = 43.5\text{ ergs s}^{-1}$ ), and the composite was assigned the lowest luminosity ( $\log(L_{5.6\text{ }\mu\text{m}}) = 44.7\text{ ergs s}^{-1}$ ) of the objects in the highest luminosity bin. These scaled spectra were then added together to produce Fig. 10. Even in this best-case scenario, there are no prominent PAH features visible in the residual spectrum made by subtracting the best-fitting most luminous composite model from the composite+PAH-feature spectrum (both are not detected above  $2\sigma$ ). When we increase the luminosity of the model PAH features by a factor of 2.5 (Fig. 10), the  $6.2$  and  $11.3\text{ }\mu\text{m}$  complexes become detectable at the  $2$  and  $3\sigma$  level, respectively. Assuming that PAH luminosity is correlated with the star formation rate (Schweitzer et al. 2006), this suggests there could be a non-negligible amount of star formation activity ‘hiding’ in the mid-IR composite of our most luminous quasar spectra.

#### 4.3 Narrow lines

From Fig. 11 it is clear that the EWs of the narrow-line and dust features are decreasing with luminosity, consistent with Hao et al. (2007) (with the exception of  $[\text{S III}]$ ). The EW is a measure of how the strength of the line compares to the continuum, and is only physically meaningful if the continuum source is the same as the ionizing source. In the case of the MIR spectra of quasars, this is not the case. The narrow-line region (NLR) is being ionized by the UV through soft X-ray radiation from the accretion disc while the MIR continuum is thermal emission from dust on much larger scales than the accretion disc with temperatures of the order of  $\sim 100$  K.

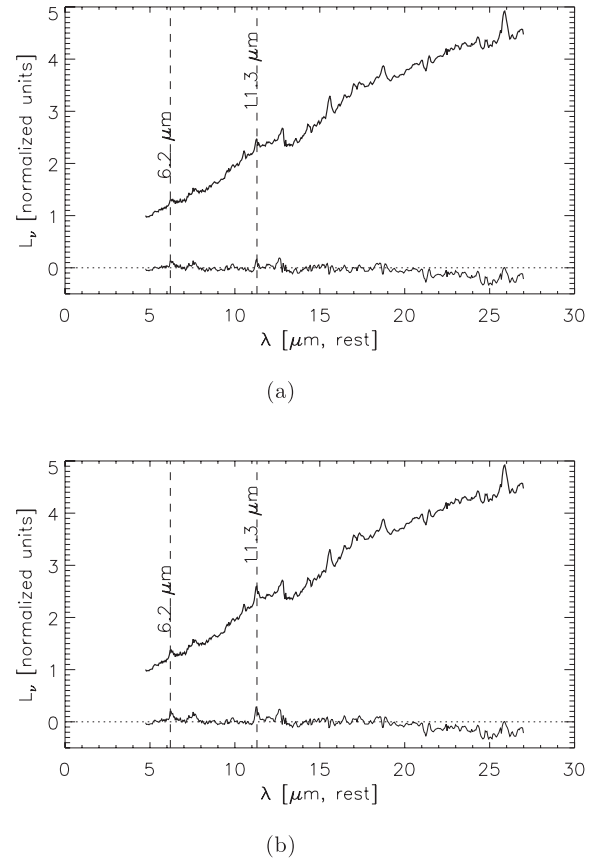


**Figure 10.** (a) The model PAH features for the lowest luminosity template (with synthetic noise) added to the most luminous template. Residuals between the model fit of Fig. 8 and the PAH-added template straddle the dashed line. The PAH features are not detectable in the residuals above  $2\sigma$  (i.e. they do not stand out significantly against the background noise). (b) The PAH features from the lowest luminosity composite have been scaled up in luminosity by a factor of 2.5. Here the  $6.2$  and  $11.3\text{ }\mu\text{m}$  complexes are detected at  $2$  and  $3\sigma$ , respectively. Given that the PAH emission is assumed to be powered by young stars, the host galaxies of the most luminous quasars could be actively star forming. The lack of detected PAH emission in the most luminous quasar template does not preclude active star formation (which powers PAH emission) in their host galaxies at the same level observed in the less luminous quasar templates.

K. Considering this, there are three possible causes of the so-called MIR Baldwin effect.

- (i) As the continuum strengthens, the lines themselves are weakening (i.e. the NLR contains less gas with increasing quasar luminosity).
- (ii) The lines are maintaining the same strength (in terms of luminosity), but are being ‘washed out’ in the strengthening continuum of higher luminosity objects (i.e. the NLR does not change with increasing quasar luminosity).
- (iii) The lines are getting stronger, but are not keeping pace with the increasing power in the continuum (i.e. the NLR is scaling with increasing quasar luminosity, but the scaling is not linear).

Netzer et al. (2004) suggested that the reason that narrow lines have decreasing EW with increasing continuum luminosity is that the NLR ‘disappears’ in some high-luminosity quasars, and the effect of averaging spectra with no narrow lines present to those with narrow lines artificially decreases the EW. This hypothesis is supported by observed-frame near-IR observations of  $[\text{O III}] \lambda 5007\text{ }\text{\AA}$ ,

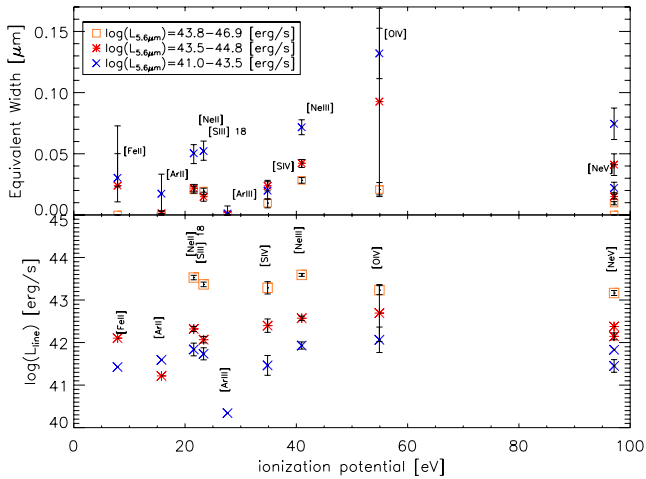


**Figure 11.** EWs (top) and line luminosities (bottom) of the narrow-line features with their estimated errors plotted against the ionization potential. The data corresponding to the template containing the most luminous objects are marked in salmon squares. The next most luminous template is marked with red asterisks, with the least luminous template indicated by blue crosses. While the EWs of the narrow lines systematically decrease with increasing  $L_{5.6\mu\text{m}}$  luminosity, the luminosity in each line is still increasing with increasing continuum luminosity.

using a luminous ( $\log(L_{5100\text{\AA}}) = 45.77\text{--}47.38$  [ergs s<sup>-1</sup>]), high-redshift sample of 29 quasars where they observed a third of their sample to have either absent or very weak [O III] emission (see Netzer et al. 2004 for further discussion). They speculated that the zone of [O III] emission in luminous quasars could be at distances beyond the extent of the host galaxy ISM. To test if this effect is also seen in our lower luminosity (in comparison to Netzer et al. 2004) sample, we looked at how the luminosity of [Ne v] 14  $\mu\text{m}$  scaled with the  $L_{5.6\mu\text{m}}$  continuum luminosity. [Ne v] 14  $\mu\text{m}$  is a good probe of the NLR because its high ionization potential (of 97 eV) minimizes the potential contribution from star formation in the host galaxy. Additionally, MIR lines are less sensitive to extinction by dust compared to optical lines. In order to obtain a luminosity from our normalized templates, we needed an estimate of how the line strengths compare from template to template. To do this, we integrated the PAHFIT-generated Gaussians for each line, and multiplied that by the relative normalized luminosity at the appropriate continuum point for each line, and then multiplied by the median  $L_{5.6\mu\text{m}}$  in that luminosity bin (see Table 3). However, we find the continuum is not well fitted in the region around the [O IV] ( $\sim 25\mu\text{m}$ ) line for the most luminous objects (see the top panel of Fig. 8), and so the line luminosities in that luminosity bin are likely underestimated. To account for this, we measured the luminosity in the [O IV] line for the most luminous composite by using a linear fit to the local continuum and fitting a Gaussian to the line. We found the power in each line is still increasing with luminosity (Fig. 11). Although the continuum is outpacing the individual lines, the lines are still getting stronger. This is consistent with the NLR becoming larger with increasing continuum luminosity. However, Netzer et al. (2004) observed more luminous objects than we did. We may just be constraining the limiting luminosity, up to which the NLR does not ‘disappear’.

The bottom panel of Fig. 11 demonstrates that the NLR is growing with increasing continuum luminosity. We want to determine if the scaling relation we find between the luminosity in various forbidden lines and the 5.6  $\mu\text{m}$  continuum luminosity is consistent with what

**Table 3.** MIR spectral feature luminosity.

Feature	$\lambda^a$ ( $\mu\text{m}$ )	IP <sup>b</sup> (eV)	High luminosity (erg s <sup>-1</sup> )	Intermediate luminosity (erg s <sup>-1</sup> )	Low luminosity (erg s <sup>-1</sup> )
H2 S(7)	5.49		42.97	41.76	40.51
H2 S(6)	6.06		43.07	41.50	40.69
H2 S(5)	6.89			41.40	40.93
[Ar II]	6.97	15.76		41.21	41.59
H2 S(4)	7.98			41.36	41.69
[Ar III]	8.97	27.63			40.34
H2 S(3)	10.52		43.14	41.88	41.49
[S IV]	12.31	34.79	43.28	42.39	41.46
H2 S(2)	12.82		43.11	41.05	40.86
[Ne II]	14.31	21.56	43.52	42.32	41.83
[Ne v] 14	14.31	97.11	43.16	42.14	41.45
[Ne III]	15.57	40.96	43.59	42.57	41.93
H2 S(1)	17.06		42.69	41.74	41.56
[S III]	18.72	23.33	43.36	42.06	41.73
[Ne v] 24	24.34	97.11		42.37	41.82
[O IV]	25.86	54.93	43.56 <sup>c</sup>	42.69	42.06
[Fe II]	26.04	7.87		42.10	41.42

*Note.* Line luminosities calculated for model outputs from PAHFIT for each luminosity template. Blank spaces indicate the feature was not detected by PAHFIT.

<sup>a</sup>Wavelengths are the best-fitting values from PAHFIT.

<sup>b</sup>Ionization potentials taken from Cox (2000).

<sup>c</sup>Calculated from fitting the local continuum around [O IV] because the PAHFIT model was overpredicting the continuum at longer wavelengths. This value is used for Figs 12–14.

would be expected. First, we must determine what the expected scaling relation should be, i.e. how does the number of ionizing photons change with increasing 5.6  $\mu\text{m}$  continuum luminosity? For this calculation, we selected three forbidden lines present in all three templates. We chose [Ne v] 14  $\mu\text{m}$  because of its high ionization potential,  $IP = 97$  eV, which is unlikely to be contaminated by star formation in the host galaxy. In addition, we use [Ne III] ( $IP = 41$  eV) and [O IV] ( $IP = 55$  eV) as all three lines are strong in all three composites, and cover a range of ionization potentials.

To determine the number of ionizing photons for each species, we integrated modified SEDs based on SEDs from Krawczyk et al. (2013) and the  $\alpha_{\text{ox}}$  relation (i.e. the anti-correlation between the luminosity at 2500  $\text{\AA}$  and 2 keV). We justify using the same SED for each template because the shape of the SED does not vary significantly from the optical to UV range as a function of luminosity. Each SED is scaled to the median value of  $L_{5.6\mu\text{m}}$  in each luminosity bin. All subsequent values used for integration are taken from these scaled SEDs. We used the luminosity at 2500  $\text{\AA}$  to estimate the 2 keV luminosity using equation (5) of Just et al. (2007). We interpolate between the Lyman limit and 2 keV with a fixed power law. This assumption could be inaccurate for calculating the ionizing flux, as the shape of the extreme UV is not known, and may be a function of luminosity or accretion rate (see discussion in section 6 of Krawczyk et al. 2013). However, we can constrain some behaviour of the EUV by examining narrow-line flux ratios using species which probe different ionization potentials. We measured how [Ne v]/[Ne III], [Ne III]/[Ne II] and [O IV]/[S III] change with 5.6  $\mu\text{m}$  luminosity. Fig. 12 shows that the line ratios do not change significantly across luminosity (within the uncertainties). Therefore, we conclude that while we may be underestimating the ionizing flux in all luminosity bins, there is no evidence for a change



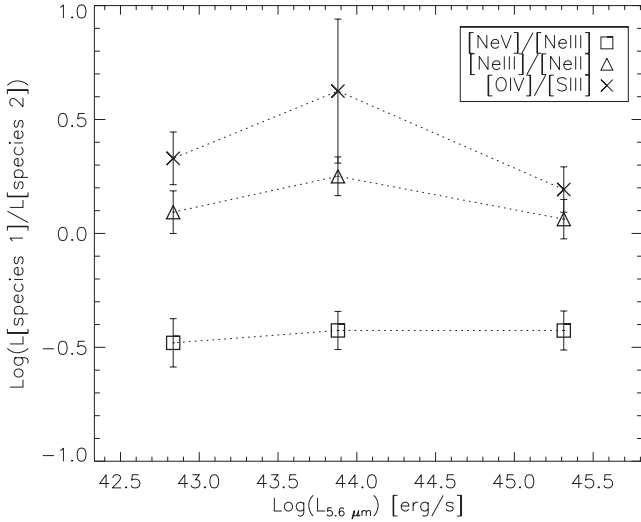


**Figure 12.** Line ratios of several MIR species ([Ne v], [Ne iii], [Ne ii], [O iv] and [S iii], plotted against the median 5.6  $\mu\text{m}$  continuum luminosity of each template). The ratios involving Ne will be less sensitive to differences in abundances, and these are quite flat, indicating that the shape of the EUV does not change significantly with luminosity.

in the continuum shape as a function of luminosity between 41 and 97 eV.

With our modified SEDs in hand, we needed to determine appropriate upper integration limits for each species. To do this, we calculated the energy at which the cross-section for ionization would decrease to half of its maximum (which occurs at the ionization energy). The calculated ranges are 41–68 eV, 55–102 eV and 97–147 eV for [Ne iii], [O iv] and [Ne v], respectively. The relationship between the number of ionizing photons and the 5.6  $\mu\text{m}$  continuum luminosity can be found in Fig. 13. We find that for lower ionization species, the number of ionizing photons rises more steeply with increasing 5.6  $\mu\text{m}$  luminosity, than for higher ionization species. This

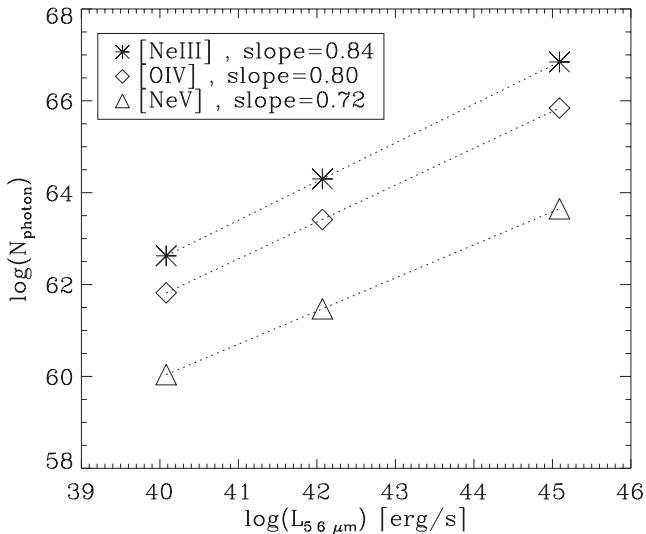


**Figure 13.** Number of ionizing photons integrated from a modified Krawczyk et al. (2013) SED, plotted against the median 5.6  $\mu\text{m}$  continuum luminosity of each template. The slopes for each linear fit are also provided in the plot. The number of ionizing photons increases more steeply with increasing continuum luminosity for the lower ionization species, as expected given the luminosity dependence of  $\alpha_{\text{ox}}$ .

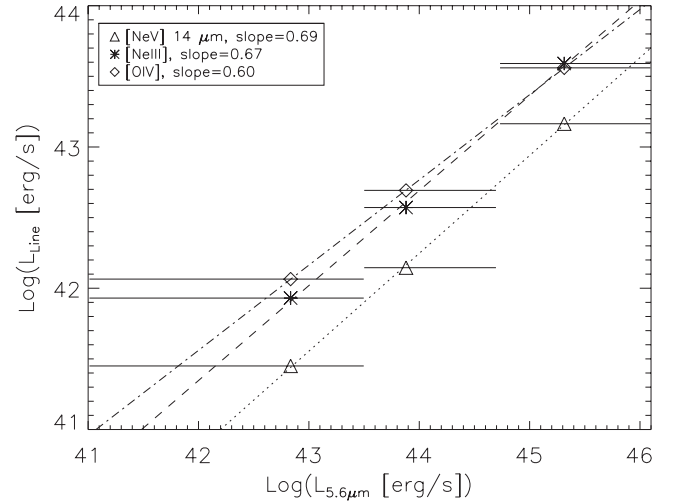


**Figure 14.** [Ne v], [Ne iii] and [O iv] line luminosity plotted against the continuum luminosity at 5.6  $\mu\text{m}$ . [Ne v] is chosen because of its high ionization potential, limiting the contamination by star formation in the host galaxies. [Ne iii] and [O iv] are chosen as they are strong lines present in all composites, and probe different ionization potentials. Horizontal bars indicate the luminosity range of the objects which contributed to that template. Dashed, dotted and dot-dashed lines are the linear fits to the points. The empirical slope for [Ne v] of 0.69 is very close to the theoretical slope of 0.72 in Fig. 13, and therefore we find no evidence for a ‘disappearing’ NLR as probed by these lines.

expected scaling relation assumes the gas densities and ionization parameters of the NLR gas are similar in all objects. All species had predicted slopes within the range of 0.72–0.84. We plotted the line luminosities of [Ne v], [O iv] and [Ne iii] against the 5.6  $\mu\text{m}$  continuum luminosity (Fig. 14), including linear fits to each species, with observed slopes ranging between 0.60 and 0.69. These best-fitting values fall below the expected range, but given the uncertainties, we consider them to be consistent. In addition, [Ne iii] may have a significant contribution from star formation in the host, especially in the lower luminosity objects with relatively more power coming out in X-rays; this would have the effect of reducing the slope. [Ne v] is not expected to have a strong contribution from star formation, and we find the slope of Fig. 14 to be very close to the predicted slope of Fig. 13. In the stratified picture of the NLR, the more highly ionized gas is located closer to the ionizing source, and will have a smaller volume filling factor than that of lower ionization species. In the case of lower ionization species (with respect to [Ne v] with  $IP = 97$  eV) such as [O iv] ( $IP = 55$  eV), the ISM of the host galaxy could be exhausted at the distance where the appropriate ionization parameter gas should be located. That is, as the appropriate ionization zone moves farther out in more luminous objects, it can extend beyond the region of the host galaxy with any appreciable ISM (Netzer et al. 2004). However, we do not see this effect. Therefore, the NLR is scaling as expected in all three lines.

## 5 DISCUSSION

The primary differences between the three templates can be attributed to host galaxy contamination. The large fraction of low-luminosity objects makes it more likely that host galaxy contamination will be significant in the low- and intermediate-luminosity templates; at low luminosities, the quasar contributes a smaller fraction of the total light and the host galaxy begins to dominate the spectrum. The PAH emission is likely from star formation in the

host galaxy, and is not from the region excited by the accretion disc in the vicinity of  $R_{\text{sub}}$ , as the hard ionizing radiation from the quasar would destroy PAHs. The PAH features are most prominent when the MIR continuum beyond  $20\ \mu\text{m}$  is at its reddest in the least luminosity template, suggesting the presence of colder dust in the low-luminosity objects relative to the high-luminosity objects. The continuum emission at the red end of the MIR spectrum (beyond  $20\ \mu\text{m}$ ) is likely from cooler dust heated by star formation, as a turnover in continuum emission is expected in the case of a pure AGN (Deo et al. 2009). This is consistent with the results of Schweitzer et al. (2006), who studied a sample of 26 PG quasars, 11 of which show the  $7.7\ \mu\text{m}$  PAH feature. The 11 quasars which exhibited strong PAH emission had enhanced FIR emission, and stronger emission from low excitation lines, indicative of active star formation. They also find the silicate emission feature at  $10\ \mu\text{m}$  to be weaker in quasars with detected PAH features; this seems to suggest that the star formation is contributing a large fraction of the overall light, making typical quasar features (e.g. silicates in emission) less prominent due to host galaxy contamination. This is consistent with our understanding that at lower luminosities, the host galaxy is contributing to a larger fraction of the total light, ‘washing’ out the quasar.

To illustrate the host galaxy contamination in the least luminous template, we normalized the PAHFIT model continuum from the most luminous template to the  $5\ \mu\text{m}$  intensity in the least luminous template and subtracted them (Fig. 15). Under the assumption that the continuum from the most luminous template is more representative of the intrinsic quasar continuum, the residuals should reflect the host galaxy contribution (specifically from star formation in the host). We overplotted a galaxy starburst template from Smith et al. (2007, their template 3), and normalized the template to the  $12.7\ \mu\text{m}$  complex of the residuals. The Smith et al. (2007) template does a

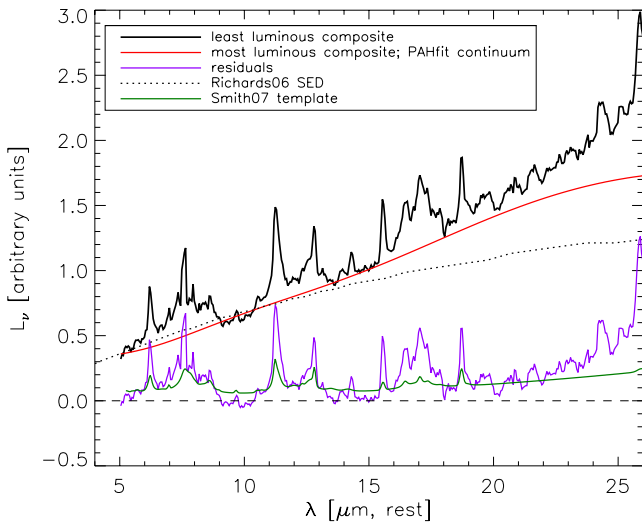


**Figure 15.** Comparison of the continuum of the most luminous template to the least luminous template. The PAHFIT model continuum of the most luminous template (solid red line) was normalized to the least luminous template at  $5\ \mu\text{m}$  (solid black line). The Richards et al. (2006b) SED (dotted black line) is overplotted for comparison. The residuals from the subtraction of the PAHFIT model continuum (solid purple line) are above the 0.0 line (dashed black line). A starburst galaxy template from Smith et al. (2007; solid green curve) is normalized to the  $12.7\ \mu\text{m}$  complex in the residuals. The features in the residuals can largely be accounted for by star formation in the host galaxy; this suggests that the underlying quasar continuum is the same for all luminosity templates.

satisfactory job of reproducing many of the main features of the spectrum, and the overall shape. We would not expect the starburst template to fit our residuals perfectly, as star-forming galaxies do not have identical SEDs, but instead exhibit a range of characteristics. Also included in Fig. 15 is the Richards et al. (2006a) quasar SED normalized to the continuum model from the most luminous template. Our model continuum matches well to the Richards et al. (2006a) at shorter wavelengths.

Considering the lack of PAH emission, together with an expected turnover in continuum in the red end of the MIR (Mor & Netzer 2012), and the results of Fig. 15 we suspect the most luminous template is representative of the true MIR spectrum of a quasar. The MIR quasar spectrum is marked by the presence of coronal lines with a range of ionization states, solid-state silicate emission features, and a hot dust bump in the near-IR (from species such as graphite).

## 6 SUMMARY AND CONCLUSIONS

(i) We have generated high S/N MIR templates from 184 quasars using archival *Spitzer* IRS data to bring out common but faint features in typically low S/N MIR quasar spectra. We also constructed three luminosity-binned templates by ordering, and dividing the sample according to the luminosity at  $5.6\ \mu\text{m}$ .

(ii) Because of the observed change in continuum, paired with the presence/absence of PAH features in the template, we hypothesize that the most luminous template is more representative of the intrinsic quasar spectrum. The other templates have much more host galaxy contamination due to the relatively low luminosity of their AGNs which thus contribute a smaller fraction of the combined MIR emission.

(iii) In the luminosity-binned templates, we note several trends with increasing luminosity: the EWs of the narrow-line and PAH features decrease, the luminosity in each narrow line increases, and the continuum flattens beyond  $20\ \mu\text{m}$ . The decrease in EW of the narrow lines with increasing luminosity is consistent with similar findings of a MIR Baldwin Effect; however, the EW is not a meaningful metric to use in the MIR because the ionizing continuum is in the UV to EUV, not in the MIR. We therefore recommend the line luminosity as a more meaningful metric.

(iv) PAH features are not detected in the most luminous template. We interpret this to imply that quasars are not the primary heaters of PAHs, and the PAH emission is likely from star formation in the host galaxy and does not scale with the AGN luminosity. More luminous starbursts are required to be detectable with a luminous AGN continuum.

(v) Silicate features at  $10$  and  $18\ \mu\text{m}$  are seen in emission, but only in the most luminous template. A ‘bump’ around  $3\ \mu\text{m}$  is present in the most luminous template, which is likely from graphites (or other species with a high sublimation temperature) located closer to the central engine which may or may not be unique to the high-luminosity template given the lack of redshift coverage in the lower luminosity templates.

(vi) Using the luminosity of  $[\text{Ne V}]$ , a high ionization MIR line insensitive to extinction and star formation in the host galaxy, we probe the size of the NLR and find it to be scaling as expected with the continuum luminosity.

## ACKNOWLEDGEMENTS

We thank the Natural Science and Engineering Research Council of Canada and the Ontario Early Research Award Program for

supporting this work. ARH was supported by an Ontario Graduate Scholarship. GTR acknowledges the generous support of a research fellowship from the Alexander von Humboldt Foundation at the Max-Planck-Institut für Astronomie and is grateful for the hospitality of the Astronomisches Rechen-Institut. We would like to thank Aycha Tammour and Jan Cami for helpful discussions. Finally, we would like to thank the anonymous referee for helpful comments that improved the presentation of this paper.

## REFERENCES

- Abazajian K. N. et al., 2009, *ApJS*, 182, 543  
 Antonucci R., 1993, *ARA&A*, 31, 473  
 Baldwin J. A., 1977, *ApJ*, 214, 679  
 Barvainis R., 1987, *ApJ*, 320, 537  
 Brandl B. R. et al., 2006, *ApJ*, 653, 1129  
 Cox N. A., 2000, *Allen's Astrophysical Quantities*, 4 edn. AIP Press, New York  
 Dasyra K. M., Ho L. C., Netzer H., Combes F., Trakhtenbrot B., Sturm E., Armus L., Elbaz D., 2011, *ApJ*, 740, 94  
 Deo R. P., Richards G. T., Crenshaw D. M., Kraemer S. B., 2009, *ApJ*, 705, 14  
 Deo R. P., Richards G. T., Nikutta R., Elitzur M., Gallagher S. C., Ivezić Ž., Hines D., 2011, *ApJ*, 729, 108  
 Edelson R. A., Malkan M. A., 1986, *ApJ*, 308, 59  
 Elitzur M., Shlosman I., 2006, *ApJ*, 648, L101  
 Elvis M. et al., 1994, *ApJS*, 95, 1  
 Gallagher S. C., Richards G. T., Lacy M., Hines D. C., Elitzur M., Storrie-Lombardi L. J., 2007, *ApJ*, 661, 30  
 Genzel R. et al., 1998, *ApJ*, 498, 579  
 Hao L. et al., 2005, *ApJ*, 625, L75  
 Hao L., Weedman D. W., Spoon H. W. W., Marshall J. A., Levenson N. A., Elitzur M., Houck J. R., 2007, *ApJ*, 655, L77  
 Hatziminaoglou E. et al., 2005, *AJ*, 129, 1198  
 Hewett P. C., Wild V., 2010, *MNRAS*, 405, 2302  
 Higdon S. J. U. et al., 2004, *PASP*, 116, 975  
 Houck J. R. et al., 2004, *ApJS*, 154, 18  
 Just D. W., Brandt W. N., Shemmer O., Steffen A. T., Schneider D. P., Chartas G., Garmire G. P., 2007, *ApJ*, 665, 1004  
 Keating S. K., Everett J. E., Gallagher S. C., Deo R. P., 2012, *ApJ*, 749, 32  
 Keremdjiev M., Hao L., Charmandaris V., 2009, *ApJ*, 690, 1105  
 Konigl A., Kartje J. F., 1994, *ApJ*, 434, 446  
 Krawczyk C. M., Richards G. T., Mehta S. S., Vogeley M. S., Gallagher S. C., Leighly K. M., Ross N. P., Schneider D. P., 2013, *ApJS*, 206, 4  
 Leboutteiller V., Bernard-Salas J., Sloan G. C., Barry D. J., 2010, *PASP*, 122, 231  
 Malkan M. A., Sargent W. L. W., 1982, *ApJ*, 254, 22  
 Mor R., Netzer H., 2012, *MNRAS*, 420, 526  
 Netzer H., Shemmer O., Maiolino R., Oliva E., Croom S., Corbett E., di Fabrizio L., 2004, *ApJ*, 614, 558  
 Pereira-Santaella M., Diamond-Stanic A. M., Alonso-Herrero A., Rieke G. H., 2010, *ApJ*, 725, 2270  
 Richards G. T. et al., 2001, *AJ*, 121, 2308  
 Richards G. T., Vanden Berk D. E., Reichard T. A., Hall P. B., Schneider D. P., SubbaRao M., Thakar A. R., York D. G., 2002, *AJ*, 124, 1  
 Richards G. T. et al., 2003, *AJ*, 126, 1131  
 Richards G. T. et al., 2006a, *ApJS*, 166, 470  
 Richards G. T. et al., 2006b, *AJ*, 131, 2766  
 Sargsyan L., Weedman D., Leboutteiller V., Houck J., Barry D., Hovhannisyan A., Mickaelian A., 2011, *ApJ*, 730, 19  
 Schneider D. P. et al., 2010, *AJ*, 139, 2360  
 Schweitzer M. et al., 2006, *ApJ*, 649, 79  
 Shen Y. et al., 2011, *ApJS*, 194, 45  
 Smith J. D. T. et al., 2007, *ApJ*, 656, 770  
 Spinoglio L., Malkan M. A., 1992, *ApJ*, 399, 504  
 Spoon H. W. W., Marshall J. A., Houck J. R., Elitzur M., Hao L., Armus L., Brandl B. R., Charmandaris V., 2007, *ApJ*, 654, L49  
 Urry C. M., Padovani P., 1995, *PASP*, 107, 803  
 Vanden Berk D. E. et al., 2001, *AJ*, 122, 549  
 Weedman D. W. et al., 2005, *ApJ*, 633, 706  
 Werner M. W. et al., 2004, *ApJS*, 154, 1

## SUPPORTING INFORMATION

Additional Supporting Information may be found in the online version of this article:

**Table 1.** *Spitzer* Object Summary.

**Table 2.** Template Spectra for all objects, and luminosity binned objects (<http://mnras.oxfordjournals.org/lookup/suppl/doi:10.1093/mnras/stt2346/-/DC1>).

Please note: Oxford University Press are not responsible for the content or functionality of any supporting materials supplied by the authors. Any queries (other than missing material) should be directed to the corresponding author for the article.

This paper has been typeset from a  $\text{\LaTeX}$  file prepared by the author.